Active optics Shack-Hartmann sensor: using spot sizes to measure the seeing at the focal plane of a telescope

P. Martinez, J. Kolb, M. Sarazin, J. Navarrete

Monthly Notices
of the
ROYAL ASTRONOMICAL SOCIETY

Mon. Not. R. Astron. Soc. **421,** 3019–3026 (2012) doi:10.1111/j.1365-2966.2012.20527.x

Active optics Shack–Hartmann sensor: using spot sizes to measure the seeing at the focal plane of a telescope

P. Martinez,[1⋆] J. Kolb,[2] M. Sarazin[2] and J. Navarrete[3]

[1] *UJF-Grenoble 1/CNRS-INSU, Institut de Planétologie et d'Astrophysique de Grenoble (IPAG) UMR 5274, Grenoble, F-38041, France*
[2] *European Southern Observatory, Karl-Schwarzschild-Strasse 2, D-85748, Garching, Germany*
[3] *European Southern Observatory, Alonso de Cordova 3107, Casilla 19001, Vitacura, Santiago, Chile*

Accepted 2012 January 9. Received 2012 January 9; in original form 2011 December 6

ABSTRACT

Nowadays, the real-time seeing estimation at the focus of a telescope is strongly emphasized because this knowledge virtually drives the dimensioning of adaptive optics systems and the operational aspects of instruments. In this context, we study the importance of using images from an active optics Shack–Hartmann (AOSH) sensor to provide accurate estimates of the seeing. At the critical location of the focus of the telescope, the AOSH sensor delivers long-exposure spot point spread functions, which are directly related to the atmospheric seeing in the line of sight. Although AOSH sensors are specified to measure not spot sizes but slopes, we show that an accurate estimation of the seeing can be obtained from AOSH images using a dedicated algorithm. We analyse the sensitivity of two algorithms and compare them to various parameters in a systematic way, demonstrating that an efficient estimation of the seeing can be obtained by adequate means.

Key words: atmospheric effects – methods: data analysis – methods: numerical – site testing.

1 INTRODUCTION

The evaluation of the seeing is important for selecting astronomical sites and for following their temporal evolution. Likewise, the estimation of the seeing is fundamental for the dimensioning of adaptive optics systems and for predicting their performance. This knowledge virtually drives the operational aspects of instruments at a telescope, and more emphasis should be given to the development and use of an accurate real-time seeing estimator at the focus of a telescope.

The atmospheric seeing is commonly measured by the differential image motion monitor (DIMM; Sarazin & Roddier 1990) in most observatories, or by alternative seeing monitors, such as the generalized seeing monitor (GSM; Ziad et al. 2000) and the multi-aperture scintillation sensor (MASS; Kornilov & Tokovinin 2001). Because it is located away from the telescope platform, such a device delivers an estimate of the seeing that can differ significantly from the effective seeing at a telescope's foci as a result of differences in pointing orientation and/or height above the ground, or local seeing bias (dome contribution). Both dome seeing and difference in height above the ground will be magnified in the context of the next generation of telescopes – the extremely large telescopes.

However, the atmospheric seeing can be deduced at the focus of a large telescope from the width of the long-exposure point spread function (PSF), assuming successive corrections to apply (e.g. turbulence outer scale, wavelength and airmass). We note that the seeing is defined at $\lambda = 500$ nm for observations at zenith. For this purpose, several types of images can be used at the critical location of the telescope foci: (i) scientific instrument images; (ii) guide probe images; (iii) active optics Shack–Hartmann (AOSH) images. At the Very Large Telescope (VLT), the focal planes are equipped with an arm used for the acquisition of a natural guide star. The light from this star is then split between a guide probe, which is used for accurate tracking of the sky, and a Shack–Hartmann wavefront sensor, which is used by the active optics to control the shape of the primary mirror.

However, in order to estimate the seeing from the full width at half-maximum (FWHM) of a PSF, we rely greatly on the exposure time, which must be long enough for the turbulence to be averaged; it is important to ensure that all representations of the wavefront spatial scales have passed through the pupil. The adequate exposure time is then dependent on pupil size and turbulence velocity, although it is commonly admitted that an exposure time of 30 s averages properly the turbulence. An exposure time shorter than 30 s will introduce significant FWHM biases. This means that the guide probe cannot be used, because exposure times are no longer than 50 ms, while images from scientific instruments do not entirely comply with the real-time aspect of the seeing estimation. Instruments are affected by an observational bias, they are unavailable for a large range of seeing conditions and they are additionally affected by the telescope's field stabilization.

The AOSH sensor delivers continuously real-time images of long-exposure spot PSFs (typically 45 s) at the same location as the

⋆E-mail: patrice.martinez@obs.ujf-grenoble.fr

scientific instruments. AOSH images simultaneously provide various data: slopes, intensities and spot sizes. When short exposures are used, the information provided by both slopes and intensities (i.e. scintillation) can be used to retrieve the Cn^2 profile using the correlations of these data from two separate stars (Robert et al. 2011). In this paper, we propose to use the spot sizes in the subapertures to retrieve the atmospheric seeing in the line of sight. In other words, we propose to use the AOSH sensor system of the telescope as a turbulence monitor to provide an accurate estimation of the seeing directly at the focus of the telescope. For this purpose, it is necessary to carefully consider the long-exposure PSF profile (to ensure precise FWHM evaluation) and to accurately derive the seeing from the estimated FWHM. In this context, we investigate the performance and limitations of two different methods that can be used to estimate the seeing from long-exposure AOSH spot PSFs. The comparison and selection of the uppermost modus operandi is a by-product of this work. Our study is carried out by means of extensive simulations, and using real data from the AOSH images obtained at the VLT. In Section 2, we describe the two different algorithms developed to retrieve the seeing from long-exposure images. In Section 3, we present our simulation hypothesis and we discuss our results. In Section 4, the real data from the VLT AOSH data base are reanalysed and compared to the synchronous image measurements obtained at the VLT (UT4) with the focal reducer and low dispersion spectrograph 2 (FORS2; Appenzeller et al. 1998). Finally, in Section 5, we present our conclusions.

2 EXTRACTING SEEING FROM SHACK–HARTMANN SPOT SIZES

An accurate estimation of the seeing from the FWHM of a turbulence-limited long-exposure PSF requires two conditions: (i) a careful assumption of the long-exposure PSF profile to ensure precise FWHM evaluation; (ii) an accurate derivation of the seeing from the estimated FWHM. In the following, we study these two conditions, and we present in detail the two dedicated algorithms.

2.1 Long-exposure PSF profile

The theoretical expression of a long-exposure PSF can be described through the expression of its optical transfer function (OTF) obtained by multiplying the telescope OTF, denoted as $T_0(\boldsymbol{f})$, by the atmospheric OTF:

$$T_a(\boldsymbol{f}) = \exp[-0.5 D_\phi(\lambda \boldsymbol{f})]. \quad (1)$$

Here, $\boldsymbol{f}$ is the angular spatial frequency, λ is the imaging wavelength and $D_\phi(\boldsymbol{r})$ is the phase structure function (Roddier 1981; Goodman 1985). This expression is miscellaneous and can be applied to any turbulence spectrum and any telescope diameter.

The analytical expression for the phase structure function in the Kolmogorov–Obukhov model can be found in Tatarskii (1961). It is expressed by $D_\phi(r) = 6.88(r/r_0)^{5/3}$, where r_0 is the coherence radius of Fried (1966). Finally, the long-exposure OTF can be expressed as

$$T(\boldsymbol{f}) = T_0(\boldsymbol{f}) \times \exp\left[-3.44(\lambda \boldsymbol{f}/r_0)^{5/3}\right], \quad (2)$$

and long-exposure PSFs are accurately described by equation (2). For a large ideal telescope with diameter $D \gg r_0$, the diffraction term T_0 can be neglected, although it cannot be neglected for AOSH subapertures of size d ($d \approx r_0$).

We note that equation (2) assumes the non-realistic behaviour of the low-frequency of the turbulence model phase spectrum. It is firmly established that the phase spectrum deviates from the power law at low frequencies (Ziad et al. 2000; Tokovinin, Sarazin & Smette 2007), and this behaviour is described in first order by an additional parameter, the outer scale L_0. The expression for the phase structure function (D_ϕ) with a finite outer scale L_0 can be found, for example, in Tatarskii (1961) and Tokovinin (2002). Because large-scale wavefronts are anything but stationary, AOSH long-exposure spot PSFs can be in first order described by equation (2), while a posteriori correction by the L_0 experimental estimate is mandatory. In the following, we examine the influence of L_0.

2.2 Seeing and FWHM

The Kolmogorov–Obukhov model predicts the dependence of the PSF FWHM ε_0 on wavelength λ and r_0:

$$\varepsilon_0 = 0.976\lambda/r_0. \quad (3)$$

Equation (3) is the definition of the seeing (assumed at $\lambda = 500$ nm, and for observations at zenith). However, the physics of turbulence implies that the spatial power spectral density (PSD) of phase distortions $W_\phi(\boldsymbol{v})$ deviates from the pure power law at low frequencies. A popular von Kàrmàn (vK) turbulence model (e.g. Tatarskii 1961; Ziad et al. 2000) introduces an additional parameter, the outer scale L_0, which describes the low-frequency behaviour of the turbulence model phase spectrum:

$$W_\phi(\boldsymbol{v}) = 0.0229 r_0^{-5/3} \left(|\boldsymbol{v}|^2 + L_0^{-2}\right)^{-11/6}. \quad (4)$$

Equation (4) is the definition of L_0, where $\boldsymbol{v}$ is the spatial frequency in m^{-1}. The Kolmogorov–Obukhov model corresponds to $L_0 = \infty$. In the vK model, r_0 describes the high-frequency asymptotic behaviour of the spectrum. In this context, the outer scale of the turbulence (L_0) plays a significant role in the improvement of image quality (i.e. FWHM) at the focus of a telescope. The image quality is different (in some cases, by a large factor, such as 30–40 per cent in the near-infrared) from the atmospheric seeing, which can be measured by dedicated seeing monitors, such as the DIMM.

The dependence of atmospheric long-exposure resolution on L_0 is efficiently predicted by a simple approximate formula (equation 5) introduced by Tokovinin (2002), and confirmed by means of extensive simulations (Martinez et al. 2010a,b), where we have emphasized that the effect of finite L_0 is independent of the telescope diameter. The validity of equation (5) has been established in a $L_0/r_0 > 20$ and $L_0/D \leq 500$ domain, where our treatment of the diffraction failed for small telescope diameters ($D < 1$ m; Martinez et al. 2010a):

$$\mathrm{FWHM} \approx \varepsilon_0 \sqrt{1 - 2.183(r_0/L_0)^{0.356}}. \quad (5)$$

As a consequence, to deduce atmospheric seeing ε_0 (at 500nm) from the FWHM of a long-exposure PSF, the correction implied by equation (5) is mandatory prior to airmass and wavelength correction. We show that this does concern even the case of small-size (d) AOSH subapertures, where $L_0 \gg d$.

2.3 Principle of the algorithms

We consider two different algorithms to extract the FWHM of a long-exposure AOSH image. These algorithms differ in their assumptions on the subaperture spot profile and in the way subaperture diffraction is taken into account, while they rely on a common preliminary step for the selection of spots retained for the analysis.

2.3.1 AOSH spot selection

For both algorithms, background estimation is performed on a corner of the image without spots, and hot pixels are set to the background. The cleanest and unvignetted spots are selected in each frame for the analysis. These extracted spots are oversampled by a factor of 2, then recentred and averaged. The averaging reduces the influence of potential local CCD defects (e.g. bad pixels, bias structures, etc.). In practice, the averaged spot is based on hundreds of selected spots.

2.3.2 OTF-based algorithm

The first algorithm, hereafter A1, was proposed by Tokovinin et al. (2007), and it is based on the long-exposure spot PSF profile defined in equation (2). The modulus of the long-exposure optical transfer function of the averaged spot is calculated and normalized. It is then divided by the following square subaperture diffraction-limited transfer function $T_0(\boldsymbol{f})$

$$T_0(\boldsymbol{f}) = [1 - (\lambda \boldsymbol{f}_x/d)] \times \left[1 - (\lambda \boldsymbol{f}_y/d)\right], \quad (6)$$

where d is the size of the AOSH subaperture. At this stage, the cut of $T(\boldsymbol{f})$ along each axis can be extracted and fitted to the exponential part of equation (2) to derive a single parameter r_0. Alternatively, it can be Fourier transformed to derive the FWHM of the resulting spot PSF profile using a two-dimensional elliptical Gaussian fit. The orientation of the long and small axes of $T(\boldsymbol{f})$ is found by fitting it with a two-dimensional elliptical Gaussian.

2.3.3 PSF-based algorithm

The second algorithm, hereafter A2, was proposed by Noethe et al. (2006), and it has been used as a diagnostic tool at the VLT since 2010 May. A2 relies on the assumption that AOSH spots can be described by the following rotationally symmetric PSF profile

$$F(\boldsymbol{u}) \propto F_0(\boldsymbol{u}) \otimes \exp\left[-(\boldsymbol{u}/r_0)^{5/3}\right], \quad (7)$$

where $\boldsymbol{u}$ is the spatial coordinate and F_0 is the diffraction-limited PSF of the AOSH subaperture. The symbol $\otimes$ denotes the convolution product. A2 relies on an approximate PSF profile based on the analytical expression of the OTF defined in equation (2). The algorithm A2 works as follows. An initial estimation of the FWHM (hereafter θ) is derived by fitting the averaged spot profile to the exponential part of equation (7). Then, A2 approximately accounts for $F_0(\boldsymbol{u})$ by quadratically subtracting the subaperture diffraction $\theta_0 = \lambda/d$ from the estimated FWHM:

$$\mathrm{FWHM} \approx \sqrt{\theta^2 - {\theta_0}^2}. \quad (8)$$

This quadratic subtraction defined in equation (8) is justified by the assumption that the two terms of equation (7) can be approximated to Gaussian functions.

3 CALIBRATION AND RESULTS

In order to calibrate and compare these two algorithms, we test them with simulated AOSH images. To match our simulations to real situations, we assume identical conditions to those encountered with the AOSH system of the VLT. Assumptions for the AOSH model and atmospheric turbulence are described below. The wavelength considered in this study is 500 nm, except when the effect of the wavelength is analysed.

3.1 Simulation hypothesis

3.1.1 Shack–Hartmann model

Our simulations are based on a diffractive Shack–Hartmann model that reproduces the VLT AOSH geometry: 24 subapertures across the pupil diameter, 22 pixels per subaperture, 0.305-arcsec pixel scale, $d = D/24 = 0.338$ m. The validity of the AOSH model has been verified using several aspects, such as the plate scale, spot sizes, slope measurements and phase reconstruction.

3.1.2 Atmospheric turbulence

The atmospheric turbulence is simulated with 300 uncorrelated phase screens of dimension 3072 × 3072 pixels (i.e. a width of 45 m). The principle of the generation of a phase screen is based on the Fourier approach: randomized white noise maps are coloured in the Fourier space by the turbulence PSD function, and the inverse Fourier transform of an outcome corresponds to a phase screen realization.

The validity of the atmospheric turbulence statistic has been tested on the simulated phase screens: the values of the outer scale (L_0), Fried parameter (r_0) and seeing of the phase screens have been confirmed by decomposition on the Zernike polynomials and variance measurements over the 300 uncorrelated phase screens. In addition, the validity of the long-exposure AOSH image has been verified. Fig. 1 shows an example of a simulated AOSH image.

We have generated AOSH images through atmospheric turbulence with seeing conditions from 0.1 to 1.8 arcsec with 0.1-arcsec increments. Except when the turbulence outer scale is an open parameter, L_0 is always defined at 22 m, which is the VLT Paranal median value (see, for instance, Dali Ali et al. 2010).

3.2 Results

In this section, we provide results from the comparison of A1 and A2. The best algorithm revealed is further characterized using several important parameters. This calibration process is a necessary step prior to on-sky implementation of such a numerical tool. This

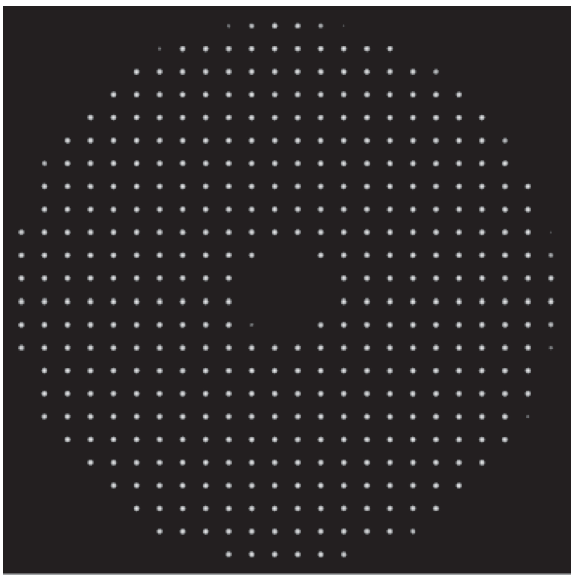

Figure 1. Simulated AOSH image based on the VLT AOSH geometry.

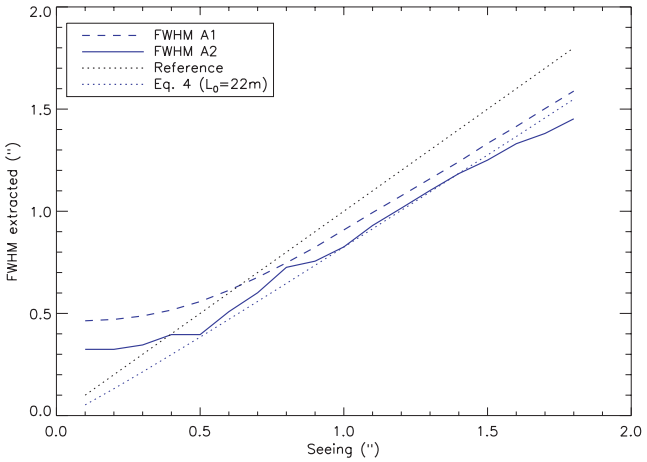

Figure 2. FWHM estimation from simulated AOSH images as a function of the seeing obtained with A1 and A2.

provides insights for the reanalysis of the VLT AOSH data base presented in Section 4.

3.2.1 *Comparison and selection of algorithms*

(i) *Response to the seeing*. Fig. 2 shows the FWHM extracted with both A1 and A2 as a function of the seeing. The black dotted line corresponds to a pure equivalence between seeing and FWHM (i.e. equation 5, assuming $L_0 = \infty$), while the black dashed line corresponds to equation (5) with $L_0 = 22$ m, which agrees with the statistic of the simulated atmospheric turbulence. The general trend of both algorithms is similar, although A2 constantly provides smaller FWHM estimations than A1. In addition, A1 provides a smoother response than A2 to the seeing; A2 exhibits irregularities in its behaviour.

The two regimes are observable. When the seeing is better than 0.6 arcsec (A1) or 0.3 arcsec (A2), the FWHM is higher than the seeing, which is likely a result of the undersampling of the Shack–Hartmann sensor (pixel scale is 0.305 arcsec). When the seeing degrades further than 0.6 arcsec (A1) or 0.3 arcsec (A2), the FWHM is smaller and asymptotically converges towards equation (5) ($L_0 =$ 22 m). This latter result is important because it demonstrates that although $d \ll L_0$, the FWHM of a long-exposure PSF obtained with very small telescope diameters (here AOSH subapertures of $\sim$30 cm) does follow equation (5). We note that the convergence of A2 to equation (5) ($L_0 = 22$ m) is inaccurate for seeing conditions worse than 1.5 arcsec.

(ii) *Subaperture diffraction removal*. A1 and A2 differ in the way they account for the subaperture diffraction. A1 is based on the deconvolution of a square subaperture OTF (equation 6), while A2 makes use of a quadratic subtraction of θ_0 (equation 8). To compare these two approaches, we assess the sensitivity of both algorithms on the subaperture diffraction. In practice, A1 and A2 have been tested on the same set of AOSH images simulated at 500 nm, while the input imaging wavelength used to feed the algorithms for removing the diffraction λ/d varies from 400 to 800 nm. Because the bandwidth centre of the wavefront sensor path can vary with the guide star type, pushing this test further with such a large range of imaging wavelengths (i.e. a wider amount of diffraction) is justified here.

The results are presented in Fig. 3 and they show that A1 and A2 behave similarly for seeing conditions $\geq$1.0 arcsec. However, in contrast to A1, for lower seeing A2 exhibits strong non-reliable irregularities. Subtracting quadratically the diffraction FWHM θ_0, as carried out by A2, is accurate as long as the effect of the diffraction is small relatively compared to the turbulence ($d \gg r_0$), and therefore it fails at large r_0 (good seeing conditions). In fact, the FWHM θ_0 varies from 0.24 to 0.49 arcsec when the wavelength varies from 400 to 800 nm. The actual AOSH PSFs are a convolution of the atmospheric blur and diffraction. Because neither of these individual broadening factors are Gaussian, the calculation of the combined FWHM as a quadratic sum of individual contributions is not accurate.

(iii) *Algorithm selection*. Considering all the aspects treated previously, it appears that A1 is more appropriate than A2. Therefore, in the following, we only consider A1 for further characterization for the sake of clarity until Section 4, where the real data obtained at the VLT with A2 are reanalysed. In the following subsections, we concentrate on the dependence of A1 on various parameters with the objective of allowing proper calibration of the algorithm. None the less, it should be noted that A2 demonstrates an identical dependence on these parameters, such that a calibration of A1 or A2 can be carried out in a similar way.

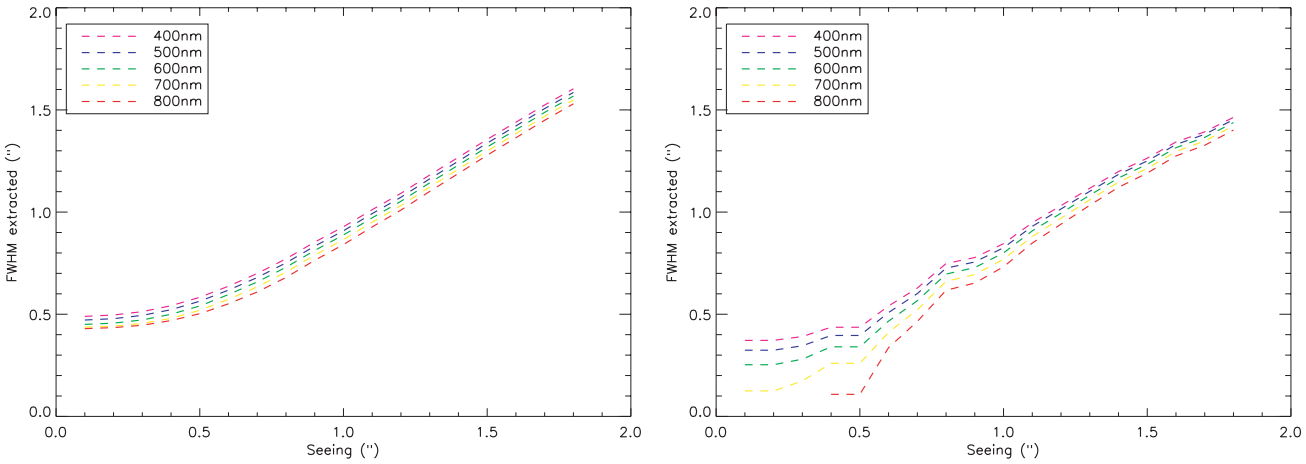

Figure 3. Subaperture diffraction removal as a function of the imaging wavelength applied to AOSH images generated at 500 nm for A1 (left) and A2 (right).

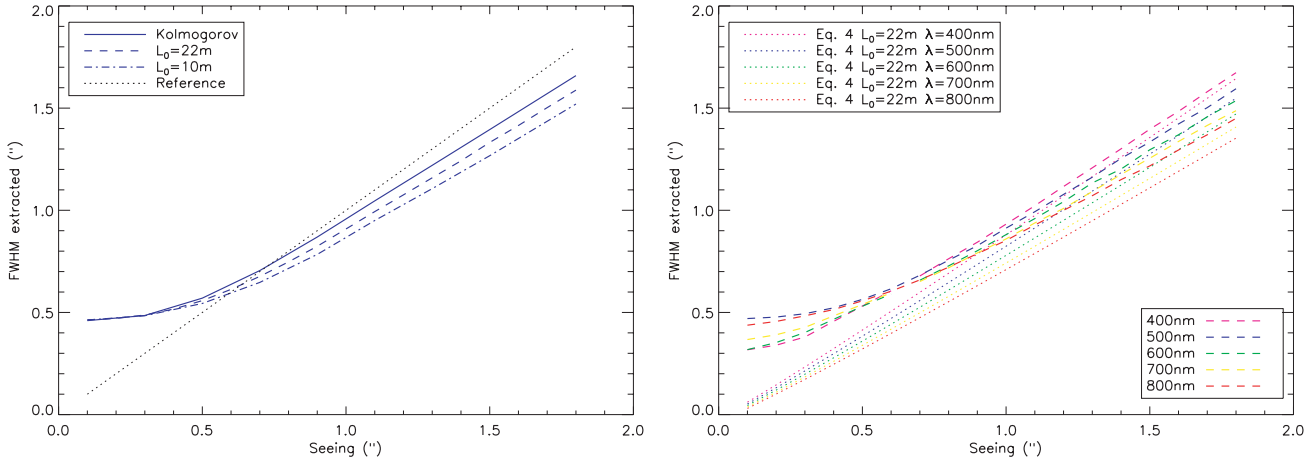

Figure 4. A1 characterization: effect of the turbulence outer scale L_0 (left) and the AOSH imaging wavelength (right).

3.2.2 *Turbulence outer scale*

Fig. 4 (left) shows the FWHM extracted with A1 as a function of the seeing for several outer-scale (L_0) values: 10 m, 22m and an infinite outer scale (although this is likely to be about 200 m because of the physical finite size of the phase screens used in the simulation). It can be seen that A1 starts to be sensitive to the outer scale for seeing higher than 0.5 arcsec. From the results presented in Fig. 4 (left), it is further established (see Section 3.2.1) that AOSH subapertures are not small enough that a spot FWHM can be approximated to ε_0 (i.e. the AOSH spot FWHM measurement does depend on the outer scale, and therefore follows equation 5).

3.2.3 *Imaging wavelength*

To analyse how the AOSH imaging wavelength affects the estimation of the seeing, we generate AOSH images for various imaging wavelengths covering the visible spectrum from 400 to 800 nm. The results are presented in Fig. 4 (right) and they indicate that an accurate knowledge of the Shack–Hartmann imaging wavelength is critical. For all wavelengths, the A1 response is constantly smooth and therefore this can be efficiently calibrated. The A1 response always asymptotically converges towards equation (5) ($L_0 = 22$ m), where we note that r_0 is wavelength-dependent. The shorter the wavelength, the faster the convergence to equation (5). This behaviour has already been reported in Martinez et al. (2010a), where we examined the validity of equation (5) with wavelength in the context of telescope images. As noticed in Section 3.2.1, and generalized here for all wavelengths, below 0.6 arcsec the impact of the AOSH pixel scale is observable. The reliability of the seeing estimation fails at very good seeing conditions when seeing $<2\times$ pixel scale (here 0.61 arcsec).

3.2.4 *Spot sampling*

To understand the asymptotical trend of the algorithm response to the seeing presented in the previous subsections, we analyse the effect of the spot sampling on the FWHM measurement. The results are presented in Fig. 5 (left), where it is shown that for a given seeing, the estimation becomes better when the sampling improves. The FWHM at 0 arcsec pixel^{-1} sampling corresponds to the theoretical values obtained with equation (5). A rough estimation indicates that 5 pixel per FWHM are required for an accurate measurement. However, spot undersampling can be calibrated and corrected.

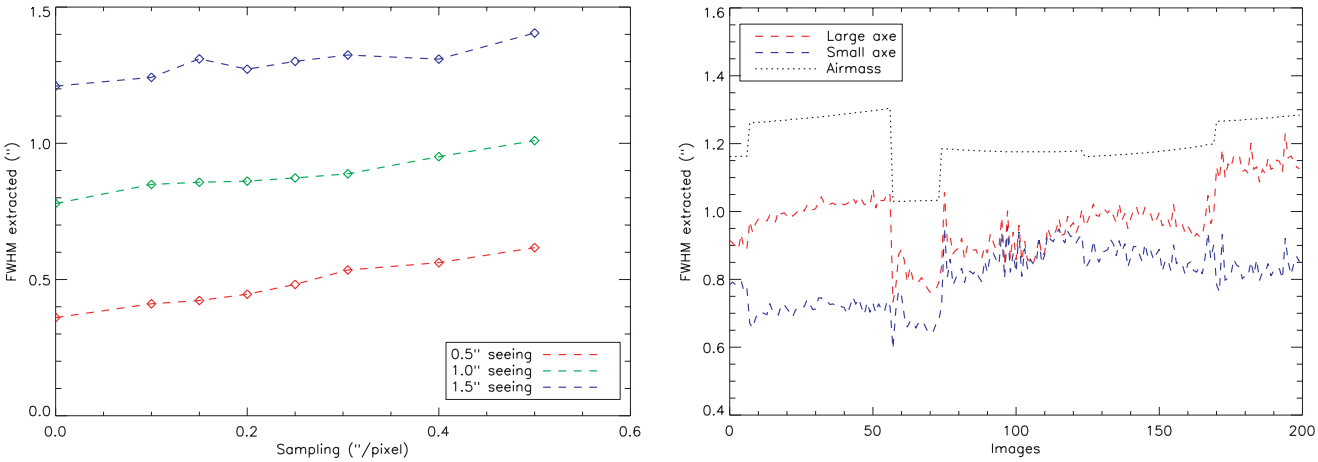

Figure 5. Left: effect of the AOSH spot sampling. Right: effect of the uncorrected atmospheric dispersion on the seeing estimation (real data).

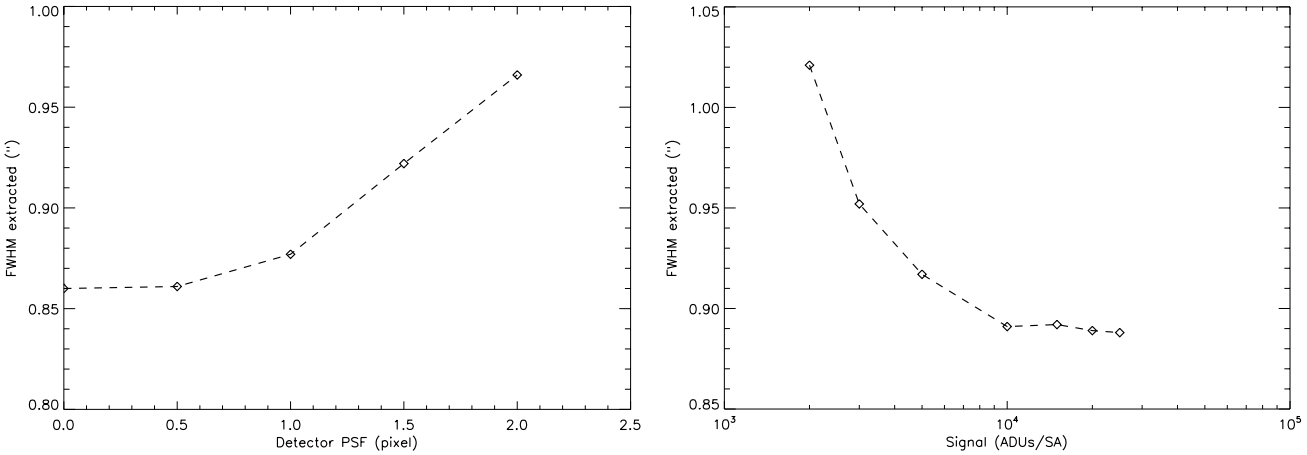

Figure 6. Left: effect of the detector PSF on the seeing estimation. Right: effect of the S/N ratio (RON = 15 ADUs) on the seeing estimation.

3.2.5 Field stabilization

The telescope field stabilization removes the low-frequency tip–tilt components generated by, among other things, wind shacking. As a consequence, the field stabilization also removes the slow turbulence, which can reduce the FWHM of a PSF image. To assess the impact of the field stabilization, we compare the FWHM measurements on simulated AOSH images, where the tip–tilt contribution (in the full telescope pupil) has been completely removed (i.e. perfect field stabilization with an infinite bandwidth), to those of AOSH images left unmodified. This test has been carried out for several seeing conditions (0.1, 0.9 and 1.8 arcsec) and outer-scale values (10 m, 22 m and the infinite case). No impact at all has been revealed except at a 0.01-arcsec level, which is negligible. The estimation of the seeing from the width of AOSH spots is therefore not sensitive to the field stabilization, which is a relevant advantage. The tip–tilt in the subaperture comes from the contribution of several low-order modes, which explains why the AOSH spot PSF FWHM is sensitive to the turbulence outer scale but not to field stabilization.

3.2.6 Atmospheric dispersion

Except for data taken at zenith, an individual spot in the AOSH image can exhibit elongation in one direction because of uncorrected atmospheric dispersion. A1 allows the estimation of FWHM in two orientations: the small and large axes. The algorithm has been tested on 200 real AOSH images obtained at the VLT-UT3 Nasmyth focus (not equipped with an atmospheric dispersion compensator) on 2010 May 12. The results of the FWHM extracted along the small and large axes are presented in Fig. 5 (right) where the airmass is also plotted. The results show that A1 does identify the elongated axis, and the ratio between both axes follows the evolution of the airmass. The difference between the two axes can be as large as 0.3 arcsec, which is substantial. The ability to distinguish between the small and large axes of the FWHM is therefore mandatory. We note that A2, by assuming a rotationally symmetric theoretical spot PSF profile (equation 7) does not allow us to differentiate between these two orientations.

3.2.7 Detector PSF

The diffusion of charges in the detector material before they are allocated to one pixel is observable as an artificial enlargement of the PSF. In most cases, the spatial response of the detector is not easy to determine. Fig. 6 (left) shows the effect of the detector PSF on the measured FWHM in the case of 1.0-arcsec seeing. We have found that the detector PSF does enlarge the AOSH spot FWHM and that the effect can be significant; it starts to be substantial from one pixel, which is larger than is usually encountered in scientific detectors, in particular those at the VLT.

3.2.8 Signal-to-noise

At the VLT, the read-out-noise (RON) level of the AOSH is above 15 ADUs, while the typical signal is about 20 000 ADUs (per subaperture). Fig. 6 (right) presents the measured FWHM in the case of 1.0-arcsec seeing as a function of the signal level (in ADUs) for a RON of 15 ADUs. It is shown that a poor signal-to-noise (S/N) ratio image enlarges the FWHM, which is evident for a signal lower than 10 000 ADUs, while for a signal higher than 10 000 ADUs, the FWHM measurements are roughly stable. The standard signal ADU level obtained at the VLT is therefore high enough to avoid any impact on the FWHM estimation, although it can be calibrated otherwise if the flux is known.

4 APPLICATION TO THE VLT AOSH DATA BASE

4.1 Correction law and error budget

To relate our simulations to real situations, we reanalysed the VLT AOSH data base obtained over the past year. At the VLT, FWHM estimates have been recorded as diagnostic information since the commissioning of the telescope, while the A2 algorithm has been used since 2010 May. As shown in the previous sections, A2 (and similarly A1) must be calibrated. From Fig. 2, it is straightforward to fit the data of A2, and to derive a correction law to transform FWHM into seeing, taking into account some of the critical parameters studied in the previous sections. Accounting for the median outer-scale value of Paranal (22 m; Dali Ali et al. 2010), the undersampling of the AOSH at the VLT and the imaging wavelength, we have found that the following equation provides an accurate estimate of seeing from A2 FWHM measurements:

$$\epsilon_0 = 1.18 \times (\mathrm{FWHM}^{1.84} - 0.15)^{1/2}. \quad (9)$$

From the sensitivity analysis of A1 (likewise A2) to various parameters, here we propose to classify the critical parameters associated with an error budget. Based on the previous systematic examination of all parameters affecting the estimation of the seeing, we can conclude that L_0, λ and the detector PSF are the major parameters to consider. All other parameters can be excluded from the error budget. This could be because they have a negligible impact (field stabilization, S/N ratio), because they have a known and constant value and can be thus calibrated (spot sampling) or because they are already considered by the algorithm (atmospheric dispersion). The Paranal median value for the outer scale is 22 m. For the error budget of this term, we consider the $\pm 1\sigma$ deviation around the median value of 22 m (11and 42 m). At the VLT, the bandwidth of the wavefront sensor path is centred around 550 nm, on average. As this can vary with the guide star type, we consider a central wavelength of 550 ± 50 nm. Hence, we assume a deviation between 500 and 600 nm. For the detector PSF term, because the value is unknown at the VLT, we consider that it is confined between our reference and ideal 0 value and 1 pixel.

We have found that the error terms (σ) can be expressed as

$$\sigma_{L_0} = 0.033 \times \epsilon_0, \tag{10}$$

$$\sigma_{\lambda} = -0.009 + 0.096 \times \epsilon_0 \tag{11}$$

and

$$\sigma_{\text{detector}} = 0.011 \times \epsilon_0. \tag{12}$$

Assuming that all terms are independent, we can therefore write the error budget of equation (9) as

$$\sigma^2_{\epsilon_0} = \sigma^2_{L_0} + \sigma^2_{\lambda} + \sigma^2_{\text{detector}}. \tag{13}$$

In contrast with A1, we note that for A2 an additional term σ_{AD} should be considered, which denotes the atmospheric dispersion impact. From this budget error, we can estimate that all these independent error sources affect the seeing derived from AOSH images at the $\sim$10 per cent level. Ideally, a drastic reduction of this error level is possible with simultaneous and instantaneous measurements of L_0, and with an accurate knowledge of the guide star type.

4.2 Application to the VLT data base

We have applied equation (9) retroactively on the VLT AOSH data base obtained at UT4. In particular, we have used a set of 6500 simultaneous FWHM measurements obtained since 2010 May with the AOSH (using A2) and the FORS2 instrument images. We note that the FWHM estimation on a long-exposure PSF from any scientific instrument follows equation (5). We also note that the FORS2 data might be biased by several parameters, including the telescope field stabilization and the accuracy of the FWHM extraction, which is based on the SEXTRACTOR software (SOURCE EXTRACTOR; Bertin & Arnouts 1996). Briefly, SEXTRACTOR is run on the reduced FORS2 images, and stars are identified based on SEXTRACTOR parameters, while their FWHMs are measured by the program through the use of a Gaussian fit applied on the data. The FWHM is afterwards extracted from the estimated Gaussian profile. The examination of the reliability of FORS2 data is beyond the scope of this paper, and therefore the comparison between AOSH and FORS2 data must be carefully considered here.

The correction to apply to the data is carried out as follows. (i) The FORS2 FWHM data are corrected by equation (5), assuming $L_0 = 22$ m (the Paranal median value), while A2 FWHM data are left uncorrected by equation (9). (ii) The FORS2 FWHM data are corrected by equation (5), assuming $L_0 = 22$ m, and the A2 FWHM data are corrected by equation (9). The results are shown in Fig. 7, where the red and blue dots correspond to (i) and (ii), respectively. Fig. 7 demonstrates that the FORS2 correction for L_0 and the AOSH correction with equation (9) bring the seeing correspondence into better agreement. This is obviously expected, as both FORS2 and AOSH deliver FWHM estimates at the same location (i.e. the focus of the UT4 telescope). This result further confirms the reliability of seeing extraction from AOSH data.

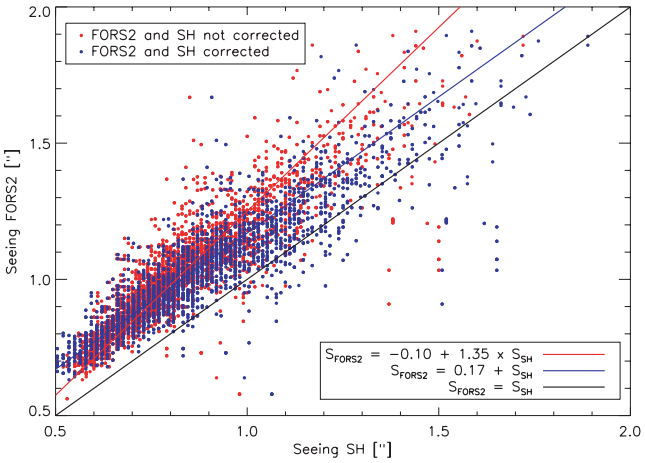

Figure 7. Simultaneous estimations of the seeing with FORS2 and the VLT AOSH data base. The AOSH data are corrected by equation (9) (blue dots) and left uncorrected (red dots). The FORS2 data are corrected by equation (5) (L_0). The best fit of each data set is also plotted (solid red and blue lines), while the black solid line represents the reference (i.e. the ideal perfect match of FORS2 and AOSH seeing estimates). Correction of FORS2 for the outer scale and AOSH correction with equation (9) bring the seeing correspondence into better agreement.

The power laws of both sets of data are provided in Fig. 7 and are also plotted for the sake of clarity. When the AOSH data are corrected by equation (9), it can be seen that the slope of the power law through the data is linear and is equal to unity, in contrast to the situation where the AOSH data are left uncorrected. Only a constant and homogeneous overestimation of FORS2 seeing remains. Such an overestimation reflects the presence of a bias, which likely finds its origin in the FWHM estimation carried out by SEXTRACTOR. For instance, long-exposure PSF profiles cannot be described by a Gaussian, and thus the calculation of the FWHM based on a Gaussian fit is not accurate. This typically induces an overestimation of the seeing at the $\sim$10 per cent level.

We note that equation (9) can be used on the VLT AOSH data base, which is temporally valid from 2010 May up to the present. From the commissioning of the VLT up to 2010 May, another correction law must be derived because another algorithm was in use. In addition, in the future, A1 should replace A2 at the VLT, and thus equation (9) will have to be readapted accordingly.

5 CONCLUSION

The AOSH sensor offers several advantages when estimating the seeing at the focus of a telescope. It delivers long-exposure PSFs and it is not affected by any observational bias (continuous real-

time seeing estimation) in contrast to scientific instruments. We also show that it is not sensitive to the telescope field stabilization.

The comparison of the two proposed algorithms has shown that the algorithm proposed by Tokovinin et al. (2007) has the advantage, which is based on the theoretical OTF expression of the long-exposure PSF. Although PSF-based and OTF-based algorithms exhibit similar general behaviour, we have found that A1 provides a smoother response than A2 to the seeing and better accounts for the subaperture diffraction and atmospheric dispersion.

We show that the estimation of the seeing from AOSH images is sensitive to several parameters but it can be calibrated. We establish that, even considering the small size of the AOSH subapertures ($\sim$30 cm), it does depend on the turbulence outer scale L_0 and therefore follows equation (5). We show that the AOSH sensor can be used to build statistics using a median value of L_0, in a real-time fashion but relying on the median L_0 value, or requiring an instantaneous measurement of L_0. We note that, in this context, several independent campaigns have converged to obtain a median value of L_0 of 22 m at Paranal (e.g. Dali Ali et al. 2010).

The VLT AOSH data base, which has been available since the commissioning of the telescope, provides spot FWHMs but not seeing information. In this context, equation (9) is required to derive the seeing information. We note that equation (9) is temporally valid until 2010 May. With these considerations in mind, the reanalysis of the past few years of the VLT AOSH data base demonstrates that there is better agreement between the seeing in AOSH and the FORS2 imager. This result further confirms the reliability of seeing extraction from AOSH images.

Finally, the qualification and calibration of the algorithm A1 are nearly completed, which clears the path to its operational implementation at the VLT for a test period of three months starting in autumn 2011. Finally, we note that more emphasis should be given to the use of closed-loop real-time AO instruments data in the near future in order to obtain the estimate of the seeing at the critical location of the focus of the telescope.

ACKNOWLEDGMENTS

The work outlined in this paper was supported by the European Commission, Seventh Framework Programme (FP7), Capacities Specific Programme, Research Infrastructures; specifically the FP7, Preparing for the Construction of the European Extremely Large Telescope Grant Agreement, Contract number INFRA-2007-2.2.1.28. We acknowledge Philippe Duhoux from the European Southern Observatory for his help with the VLT control software.

REFERENCES

Appenzeller I. et al., 1998, The Messenger, 94, 1
Bertin E., Arnouts S., 1996, A&AS, 117, 393
Dali Ali W. et al., 2010, A&A, 524, A73
Fried D. L., 1966, J. Opt. Soc. Am., 56, 1372
Goodman J. W., 1985, Statistical Optics. Wiley, New York
Kornilov V. G., Tokovinin A. A., 2001, Astron. Rep., 45, 395
Martinez P., Kolb J., Tokovinin A., Sarazin M., 2010a, A&A, 516, A90
Martinez P., Kolb J., Sarazin M., Tokovinin A., 2010b, The Messenger, 141, 5
Noethe L., Sarazin M., 2006, ESO Internal Document, 'Seeing Measurements with the Shack–Hartmann Analyser'
Robert C., Voyez J., Védrenne N., Mugnier L., 2011, contribution to conference Comprehensive Characterization of Astronomical Sites (arXiv:1101.3924)
Roddier F., 1981, Prog. Opt., 19, 281
Sarazin M., Roddier F., 1990, A&A, 227, 294
Tatarskii V. I., 1961, Wave Propagation in a Turbulent Medium. Dover, New York
Tokovinin A., 2002, PASP, 114, 1156
Tokovinin A., Sarazin M., Smette A., 2007, MNRAS, 378, 701
Ziad A., Conan R., Tokovinin A., Martin F., Borgnino J., 2000, Appl. Opt., 39, 5415

This paper has been typeset from a TEX/LATEX file prepared by the author.